

# Molecular motors robustly drive active gels to a critically connected state

José Alvarado<sup>1</sup>, Michael Sheinman<sup>2</sup>, Abhinav Sharma<sup>2</sup>, Fred C. MacKintosh<sup>2\*</sup>  
and Gijsje H. Koenderink<sup>1\*</sup>

**Living systems naturally exhibit internal driving: active, molecular processes drive non-equilibrium phenomena such as metabolism or migration. Active gels constitute a fascinating class of internally driven matter, in which molecular motors exert localized stresses inside polymer networks. There is evidence that network crosslinking is required to allow motors to induce macroscopic contraction. Yet a quantitative understanding of how network connectivity enables contraction is lacking. Here we show experimentally that myosin motors contract crosslinked actin polymer networks to clusters with a scale-free size distribution. This critical behaviour occurs over an unexpectedly broad range of crosslink concentrations. To understand this robustness, we developed a quantitative model of contractile networks that takes into account network restructuring: motors reduce connectivity by forcing crosslinks to unbind. Paradoxically, to coordinate global contractions, motor activity should be low. Otherwise, motors drive initially well-connected networks to a critical state where ruptures form across the entire network.**

One of the defining qualities of soft matter is that it is readily driven far from thermodynamic equilibrium by external stress. Driving forces such as those due to an electric field or shear drive colloidal suspensions and polymer networks into fascinating non-equilibrium patterns, including banded<sup>1,2</sup>, jammed<sup>3</sup>, and randomized steady states<sup>4</sup>. Much progress has been made in understanding such externally driven systems<sup>5</sup>. By contrast, living soft-matter systems such as cells and tissues naturally exhibit a unique form of internal driving in the form of mechanochemical activity<sup>6,7</sup>. A prominent example is the cytoskeleton, a meshwork of protein polymers and force-generating motor proteins that constitutes the scaffold of cells. In solutions of purified cytoskeletal filaments and motors, remarkable self-organized patterns have been observed<sup>8,9</sup>, inspiring theoretical work on these so-called active gels<sup>10–13</sup>.

More recently, attention has shifted to the important role of network connectivity in active gels, which can be controlled by the number of crosslinks between filaments. In weakly connected systems, motors slide filaments to form static or dynamic clusters<sup>14–17</sup>. In the opposite limit of a well-connected, elastic network, motors generate contractile stresses as they pull against crosslinks and stiffen the network<sup>10,11</sup> or cause contraction<sup>18,19</sup>. The existence of a threshold connectivity that separates these two behaviours has been proposed, because macroscopic contractions are known to occur above certain minimum values of crosslink or actin concentration<sup>15,17,18,20</sup>. We should expect remarkable critical behaviour at the threshold of contraction. Recent theoretical models predict diverging correlation length scales and a strong response to external fields<sup>21–24</sup> at the threshold of rigidity. In suspensions of self-propelled patches, critical slowing was predicted at the threshold of alignment<sup>25</sup>. Yet the threshold of contraction still remains poorly understood, and experimental evidence of criticality in active gels remains lacking.

Here, we experimentally study model cytoskeletal systems composed of actin filaments and myosin motors. We vary network

connectivity over a broad range by adding controlled amounts of crosslink protein. We show that the motors actively contract the networks into disjoint clusters that exhibit a power-law size distribution. This behaviour is reminiscent of classical conductivity percolation<sup>26</sup>, for which a power-law size distribution of clusters occurs close to a critical point. However, in sharp contrast to this equilibrium phenomenon, we observe critical behaviour over a wide range of initial network connectivities. To understand this robustness, we develop a general theoretical model of contractile gels that quantitatively accounts for our observations. In this model, motors not only contract the network, but also reduce the connectivity of initially stable networks down to a marginal structure by promoting crosslink unbinding. Below this marginal connectivity, the network no longer supports stress and the system rapidly devolves to disjoint clusters which reflect the critical behaviour of the marginal structure. Our model predicts cluster size distributions that agree well with experiment. Moreover, it predicts an inverse relationship between cluster size and motor activity, which we also confirm experimentally.

## Experiment: motors rupture networks into clusters

To resolve the interplay between motor activity and network connectivity in active cytoskeletal networks, we developed a customized assay to view entire motor-driven contraction events for up to two hours (Fig. 1a; see Methods). We control motor activity and network connectivity by varying the density of myosin motors and fascin crosslinks, respectively. These are given by the molar ratios  $R_M$  and  $R_C$  (see Methods).

To resolve the influence of network connectivity, we first prepare a series of networks with constant myosin activity ( $R_M = 0.01$ ) and gradually increasing  $R_C$ . Even at low  $R_C$ , motors contract actin networks, albeit on small length scales (Fig. 1b and Supplementary Movie S1). However, when we increase  $R_C$ , contraction occurs on a larger length scale (Fig. 1c and Supplementary Movie S2). The motors break the network up into multiple disjoint clusters. At

<sup>1</sup>FOM Institute AMOLF, Science Park 104, 1098 XG Amsterdam, The Netherlands, <sup>2</sup>Department of Physics and Astronomy, Vrije Universiteit, 1081 HV Amsterdam, The Netherlands. \*e-mail: fcm@nat.vu.nl; gkoenderink@amolf.nl

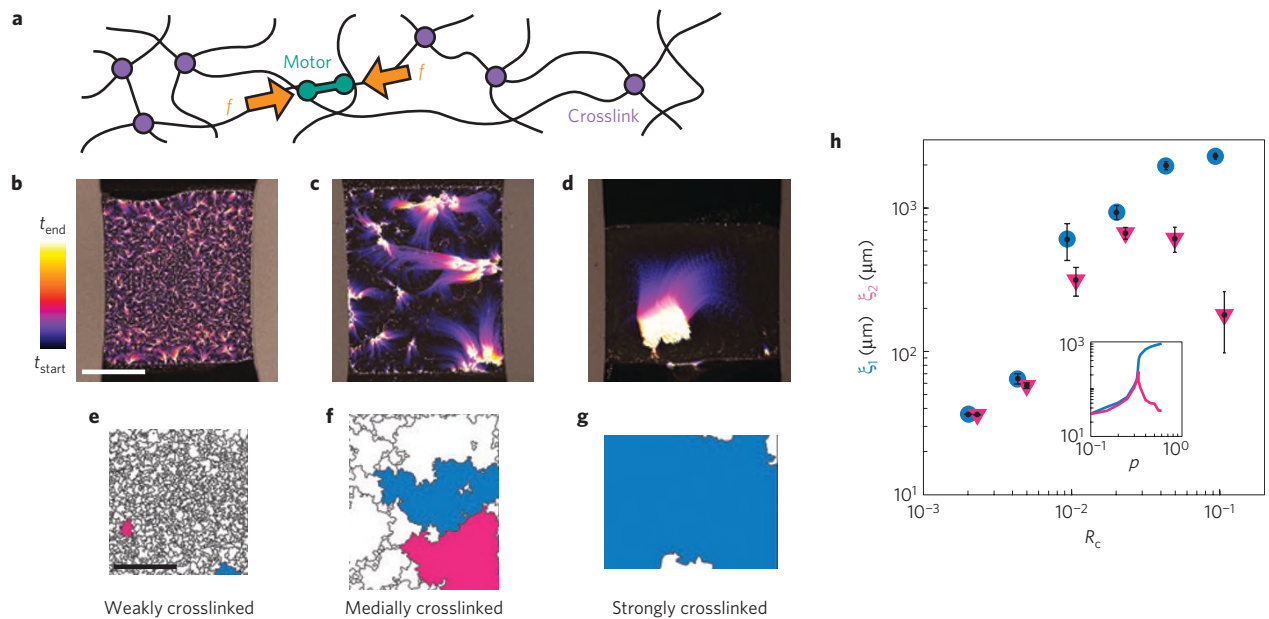


**Figure 1 | Experiments with motor-driven networks show that initial connectivity controls the length scale of contraction.** **a**, Schematic of the experiment. Actin filaments (black lines) are connected by crosslinks (purple circles), and myosin motors (green dumbbells) exert force dipoles (orange arrows) on actin filaments. **b-d**, Temporal evolution of three networks with varying amounts of fascin crosslinks  $R_C = 0.01$  (**b**);  $R_C = 0.05$  (**c**);  $R_C = 0.1$  (**d**). Actin concentration and motor molar ratio are constant: (actin) = 12  $\mu\text{M}$ ;  $R_M = 0.01$ . Colour corresponds to time according to the calibration bar (**b**, left). Times ( $t_{\text{start}}$ ,  $t_{\text{end}}$ ) in minutes after initiation of actin polymerization: **b** (2, 20); **c** (2,120); **d** (1,5). Scale bar, 1 mm. See Supplementary Movies S1-S3. **e-g**, Decomposition into clusters, delimited by black lines. Colour indicates the largest (blue) and the second-largest (pink) cluster, whose sizes correspond to  $\xi_1$  and  $\xi_2$  respectively. Note that **g** does not have a second-largest cluster because we exclude long edge domains from our analysis (Supplementary Fig. S6). **h**, Dependence of  $\xi_1$  (blue circles) and  $\xi_2$  (pink triangles) on  $R_C$ . Error bars denote standard errors of the mean for repeat experiments: 1, 6, 13, 14, 9, and 5 experiments for  $R_C = 0.002, 0.005, 0.01, 0.02, 0.05,$  and  $0.1$ , respectively. Inset: Predicted dependence of  $\xi_1$  (blue) and  $\xi_2$  (pink) on connection probability  $p$  according to percolation theory, given the experimental parameters (Supplementary Information).

still higher  $R_C$ , motor activity contracts the entire network into a single dense cluster, which often retains the square shape of the assay chamber (Fig. 1d and Supplementary Movie S3).

To quantify the effect of connectivity on the length scale of network contraction, we developed an image processing algorithm (Supplementary Movie S4) which identifies the clusters in the final image and traces their origin back in time. As shown in Fig. 1, the initial areas of each cluster are small in weakly crosslinked networks (Fig. 1e). The smallest clusters are  $\sim 30 \mu\text{m}$  in size, which corresponds to the typical distance between myosin motor clusters in the absence of crosslinks (Supplementary Fig. S1). However, the clusters increase in size when the molar ratio of crosslinks is increased (Fig. 1f). In strongly crosslinked networks, the entire network forms one cluster (Fig. 1g).

Qualitatively, the transition from local to macroscopic contraction is reminiscent of a classical conductivity percolation transition. Below this transition, a system is only locally correlated and cannot establish connections over long distances. Only above a certain critical connectivity can the system establish global correlations. To determine the extent of agreement between our experimental results and percolation theory, we investigate three key predictions<sup>26</sup>.

First, conductivity percolation theory predicts how connectivity determines the size of the largest and second-largest connected clusters. Connectivity is quantified by the probability  $p$  of creating a connection. The largest cluster (of size  $\xi_1$ ) is predicted to increase monotonically with  $p$ , whereas the second-largest cluster (of size  $\xi_2$ ) should exhibit a peak right at the conductivity percolation threshold, where  $\xi_1$  and  $\xi_2$  both approach the system size,  $L$  (Fig. 1h, inset). Our experiments agree with this prediction: the measured cluster sizes,  $\xi_1$  and  $\xi_2$ , are both small at low  $R_C$  and increase monotonically with increasing  $R_C$  until they approach the system size,  $L \approx 2.5 \text{ mm}$ , around  $R_C \sim 0.01$  (Fig. 1h). Above this threshold

connectivity,  $\xi_1$  remains close to  $L$ , whereas  $\xi_2$  decreases towards zero as the entire network contracts to one large cluster.

Second, percolation theory predicts how cluster sizes are distributed: around the critical point, we should find a power law with an exponent of  $-2$ . To test this prediction, we begin by looking for networks which satisfy  $\xi_1 \sim \xi_2 \sim L$ . We replot all measurements separately in  $\xi_1$ - $\xi_2$ -space (Fig. 2a). Because  $\xi_2 < \xi_1$  by definition, all samples are located within a triangle in  $\xi_1$ - $\xi_2$ -space. We clearly identify the samples at the triangle's peak, where  $\xi_1 \sim \xi_2 \sim L$ . We denote this peak as the critically connected regime. To the left of the peak are samples with low  $R_C$ , which we denote as the local contraction regime. To the right are samples with high  $R_C$ , which we denote as the global contraction regime.

Do the samples in the critically connected regime really exhibit critical behaviour? To test this more rigorously, we plot the entire distribution of cluster sizes (Fig. 2b). Our experiments are again consistent with percolation theory: the critically-connected regime indeed exhibits a cluster-size distribution that is statistically consistent with a power-law across more than two orders of magnitude in measured area<sup>27</sup>. The power-law exponent is  $-1.9$ , close to the predicted exponent of  $-2$ . The distributions of the other two regimes furthermore agree with percolation theory. The local contraction regime exhibits a short-tail distribution with a sharp cut-off. The global contraction regime exhibits a bimodal distribution with two well-separated length scales: the percolating cluster with size  $\xi_1 \sim L$  and other small disjointed clusters with a typical size of  $\xi_2 \ll L$ .

Third, percolation theory predicts that only systems that are close to the critical point should exhibit a power law. But this prediction is difficult to reconcile with our data: the critically connected regime in  $\xi_1$ - $\xi_2$ -space (Fig. 2a) is populated by samples which span a wide range of crosslink densities (from  $R_C = 0.01$  to

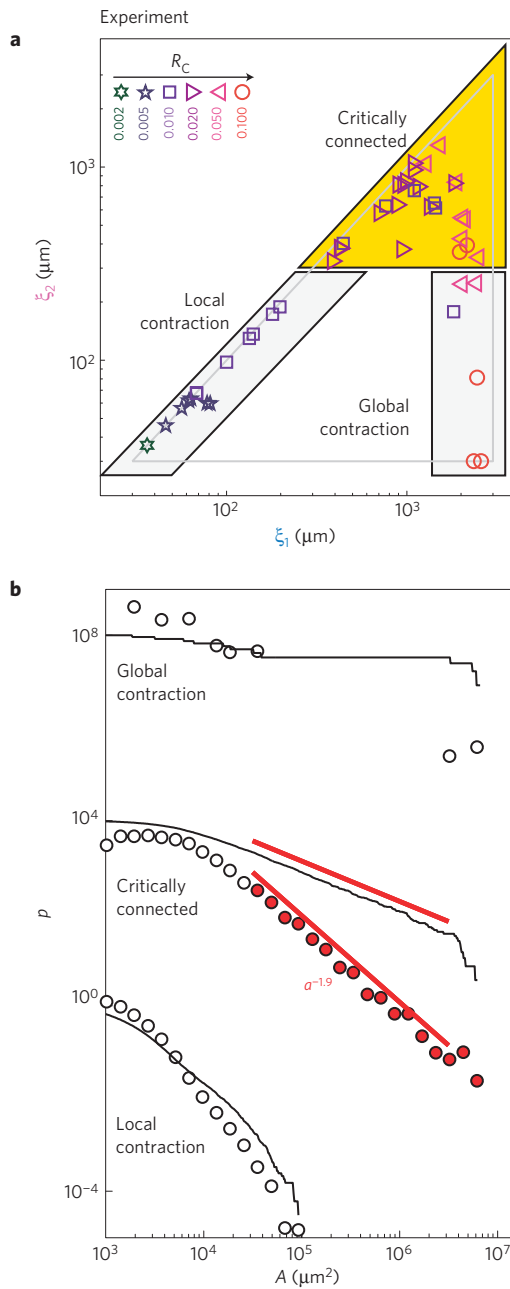


**Figure 2 | Cluster size distributions depend on network connectivity, exhibiting power-law distributions when  $\xi_1 \sim \xi_2 \sim L$ .** **a**, Scatter plot of 48 samples with different  $R_C$  in  $\xi_1$ - $\xi_2$ -space (see legend, top left). Boxes delimit different regimes: local contraction ( $\xi_1 < 300 \mu\text{m}$ ), critically connected ( $\xi_1 \geq 300 \mu\text{m}$  and  $\xi_2 \geq 300 \mu\text{m}$ ), and global contraction ( $\xi_1 \geq 1,500 \mu\text{m}$  and  $\xi_2 < 300 \mu\text{m}$ ). Two data points with  $\xi_2 = 0$  are depicted here with  $\xi_2 = 30 \mu\text{m}$ . **b**, Histogram (circles) and complementary cumulative probability distribution (solid lines) of cluster areas,  $A$ , for the three regimes. For the critically connected regime, data across more than two orders of magnitude (red circles) are statistically consistent with a power-law distribution (solid red lines) with an exponent of  $-1.91 \pm 0.06$ ,  $p = 0.52$ , where  $p > 0.1$  indicates plausible agreement with a power law (Supplementary Information). Power-law distributions appear as straight lines on a log-log plot. The visual form of the complementary cumulative probability distribution does not depend on bin size. The slope of the complementary cumulative probability distribution is equal to one plus the slope of the histogram because the histogram is the absolute value of the derivative of the complementary cumulative probability distribution.

$R_C = 0.1$ ). This is also reflected in Fig. 1h, which shows a broad  $\xi_2$ -peak that is over half an order of magnitude wide in  $R_C$ , in sharp contrast with the narrow  $\xi_2$ -peak expected from percolation theory (Fig. 1h, inset). We therefore conclude that classical conductivity percolation theory cannot provide a complete description of the physics of active, contractile networks.

### Simulation: network restructuring

Percolation theory describes a network with a fixed connectivity. This is appropriate for equilibrium fibre networks without internal driving. However, in motor-driven networks, the total connectivity can change significantly<sup>28–30</sup>. High-resolution imaging reveals that motors actively pull on network strands and disconnect them, thereby reducing connectivity (Supplementary Movie S5). Crosslinks bind only transiently ( $\sim 10$  s in case of fascin<sup>31</sup>), and their binding kinetics are stress-dependent<sup>32</sup>. There is strong evidence that unbinding of fascin crosslinks is promoted under stress<sup>33</sup>. We hypothesize that such stress-dependent binding kinetics allow motor activity to drive initially well-connected networks down towards a critically connected state.

To test this hypothesis, we develop a computational model of contractile actin-myosin networks using molecular dynamics. We model actin filaments with a planar triangular lattice of nodes connected by line segments of length  $l_0$  (Fig. 3a), which possess stretching modulus  $k$  and strain-stiffen<sup>34</sup> and buckle<sup>35</sup>. We set the average number  $z$  of line segments connected to a node (that is, the coordination number) to 4.0. Point-like crosslinks are randomly placed on nodes with probability  $p$ , which depends on crosslink concentration  $c$ . We assume first-order kinetics of crosslink (un)binding, which yields  $p = c/(1 + c)$ . We model the crosslinks by freely-hinged constraints. We model motor-induced contractile stress by pairs of forces  $f$  between nodes<sup>10,16,36–38</sup>. Every node has mobility  $\mu$  and experiences an effective, free-draining viscosity,  $\eta$ . The network evolves over time to achieve force balance at the nodes (Fig. 3b). For fixed crosslinks, network connectivity remains unchanged and  $\xi_1$  and  $\xi_2$  remain constant. We now introduce the important ingredient of network restructuring: connectivity changes via crosslink unbinding and rebinding. The unbinding rate of a crosslink  $k_{\text{off}}$  increases exponentially with the tension in the crosslink  $T$  according to Bell's law<sup>32</sup>:  $k_{\text{off}} = k_{\text{off},0} \exp(T/T_0)$ , where  $k_{\text{off},0}$  denotes the off-rate in the absence of tension, and  $T_0$  a characteristic tension (Fig. 3c). To account for rebinding, we consider the probability that an unbinding event is followed by a rebinding event at the same location before filaments are separated, which is given by  $\exp(-ck_{\text{on}}d/T\mu)$ , where  $d$  is an effective distance on the order of the mesh size over which filaments move with velocity equal to  $T\mu$  and  $k_{\text{on}}$  is the binding rate of a crosslink. The effective unbinding rate is thus given by

$$k_{\text{off}} = k_{\text{off},0} \exp(T/T_0) \exp(-ck_{\text{on}}d/T\mu)$$

By varying  $c$  across many simulations (keeping  $f$  constant), we recover the three regimes found in experiment: the local contraction (Fig. 3d,e and Supplementary Movie S6), critically connected (Fig. 3f,g and Supplementary Movie S7), and global contraction regimes (Fig. 3h,i and Supplementary Movie S8). The crosslink-dependence of  $\xi_1$  and  $\xi_2$  versus  $c$  (Fig. 3j) as well as the cluster size distributions (Supplementary Fig. S2) are consistent with experiment. Motor activity clearly broadens the  $\xi_2$ -peak: without active network restructuring (Fig. 3j, open symbols), only a narrow region (yellow stripes) around the critical point exhibits critical behaviour. With network restructuring (Fig. 3j, closed symbols), this region broadens (solid yellow box). Motor-driven network restructuring can therefore account for the surprising robustness of critical behaviour observed experimentally.

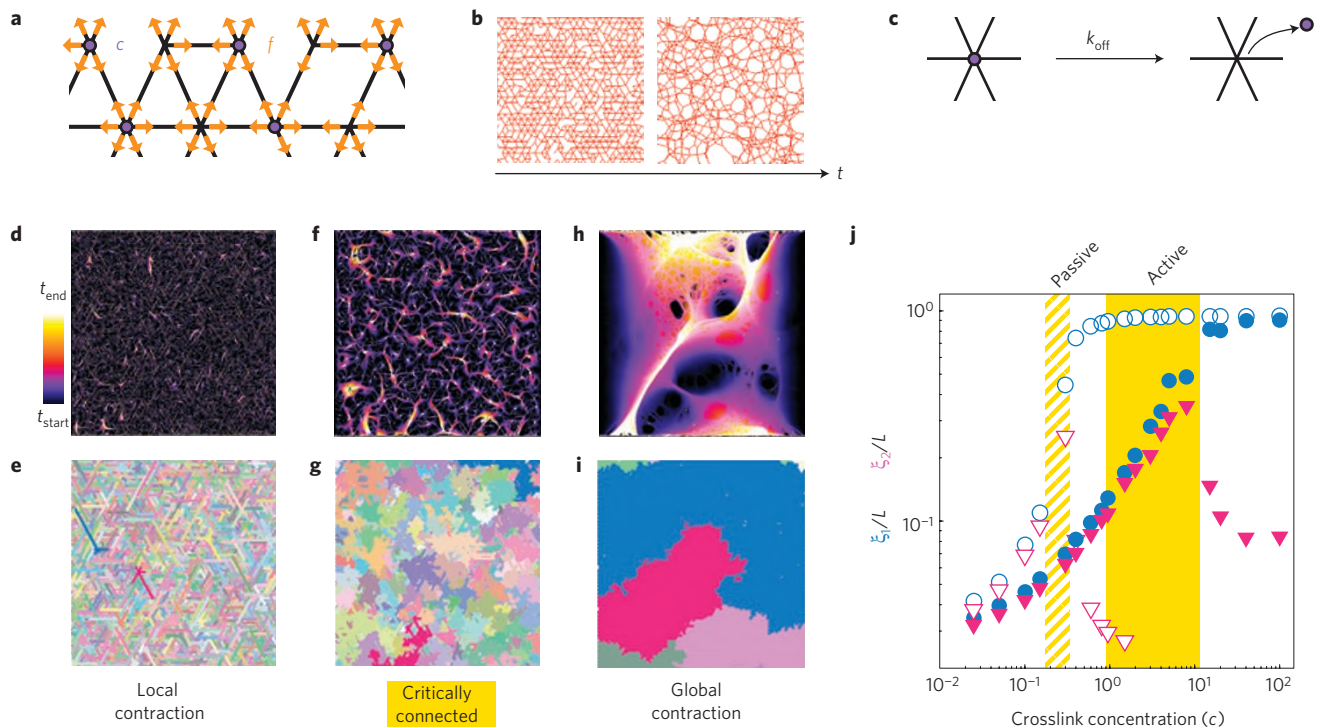


**Figure 3 | Simulations show that motors can drive initially well-connected networks to a critical state.** **a**, Schematic of the simulation. A triangular lattice of nodes, connected by line segments (black lines), contains an average of  $N$  crosslinks per node (purple circles). During the course of the simulation, pairs of nodes experience contractile forces (orange arrows) and move in response to these forces. **b**, Temporal evolution of a representative network in the absence of remodelling. **c**, Motors cause network restructuring by generating tension  $T$  on crosslinks that increases the off-rate  $k_{\text{off}}$ . **d–j**, Simulated networks exhibit behaviour consistent with experiment. See Supplementary Movies S4–S6. **d,f,h**, Temporal evolution of three networks differing in initial connectivity:  $c = 0.025$  (**d**);  $c = 3$  (**f**);  $c = 10,000$  (**h**). Force is constant:  $f/k = 50$ . Colour corresponds to simulation time according to calibration bar (**d**, left). The box size  $L$  is 100 times longer than the initial lattice size  $l_0$ . **e,g,i**, Decomposition into clusters, shaded by pastel colours. Bold colour indicates the largest (blue) and the second-largest (pink) clusters, whose sizes correspond to  $\xi_1$  and  $\xi_2$  respectively. **j**, Dependence of  $\xi_1$  (blue circles) and  $\xi_2$  (pink triangles) on crosslink concentration  $c$  across repeat simulations. Open symbols indicate values at  $t = 0$ , which corresponds to passive networks described by classical percolation theory. Closed symbols indicate values at the end of the simulation, after the network has broken up into clusters. Yellow regions correspond to values of  $c$  for which  $\xi_2 > L/10$  and the cluster size distribution exhibits a power law. Note that this region is narrow for classical percolation theory (diagonal yellow stripes) but broadens substantially in response to active internal driving (solid yellow box).

### Motors promote network restructuring

So far we have investigated the effect of connectivity in experiment and simulation ( $R_C$  and  $N$ ), but kept motor activity constant ( $R_M$  and  $f$ ). Network restructuring breaks networks into clusters because motor stresses unbind crosslinks. We thus predict that increased motor activity should lead to smaller clusters. To test this hypothesis, we simulate well-connected networks with constant  $c$  but varying motor force  $f$ . Increased force indeed leads to smaller clusters and therefore lower values of  $\xi_1$  (Fig. 4a). The cluster size distributions reflect this tendency to smaller clusters (Fig. 4b). For low force, cluster sizes exhibit two well-separated length scales, indicating global contraction. For high force, the distribution cuts off at a finite length scale.

To validate these predictions, we perform experiments in well-connected networks ( $R_C = 0.02$ ) and vary the myosin-to-actin molar ratio  $R_M$ . In agreement with the model, the length scale of contraction depends on  $R_M$ . For low  $R_M$  up to 0.002, the networks appear stationary for the entire duration of the experiment. Large-scale collective breathing fluctuations are visible, indicative of a strongly connected network, but the motors exert insufficient force to contract the network (Supplementary Movie S9). Increasing  $R_M$  to 0.005 results in a drastic change: the entire network uniformly contracts into one large cluster (Supplementary Movie S10). However, a further increase of  $R_M$  results in smaller clusters (Supplementary Movie S11). At high motor densities,  $\xi_1$  also decreases (Fig. 4c) and we recover cluster

size distributions consistent with the model's prediction (Fig. 4d and Supplementary Fig. S3). The consequence of these findings is counterintuitive: coordinated macroscopic contractions require low levels of motor activity.

### Motors nucleate many concurrent ruptures

The simulation results allow us to draw a schematic phase space of active contractile gels (Fig. 5). The global contraction regime is located at the bottom-right corner, where motor forces are low and network connectivity is high. In this limit, networks are rigid, filaments remain straight, and the network deforms affinely<sup>22</sup>. On the opposite corner, where connectivity is low and force is high, we find the local contraction regime where networks deform non-affinely and filaments are significantly bent.

We interpret these limits by considering two relevant timescales,  $\tau_{\text{off}}$  and  $\tau_{\text{relax}}$ . The first timescale is the characteristic crosslink unbinding time  $\tau_{\text{off}} = k_{\text{off}}^{-1}$ . The tension  $T$  experienced by a crosslink depends on both the motor force  $f$  and the network configuration, which can change over time. Although the full dependence of crosslink tension on motor force is complex, the qualitative behaviour is clear: when filaments are straight, motor stress does not greatly induce crosslink tension; when filaments are bent, crosslinks experience tension (Supplementary Fig. S4). We estimate  $\tau_{\text{off},0} \sim 1\text{--}10$  s based on previous work<sup>31</sup>. The second timescale,  $\tau_{\text{relax}}$ , is the time it takes for individual filaments to thermally equilibrate in response to a crosslink unbinding event. On the basis of previous

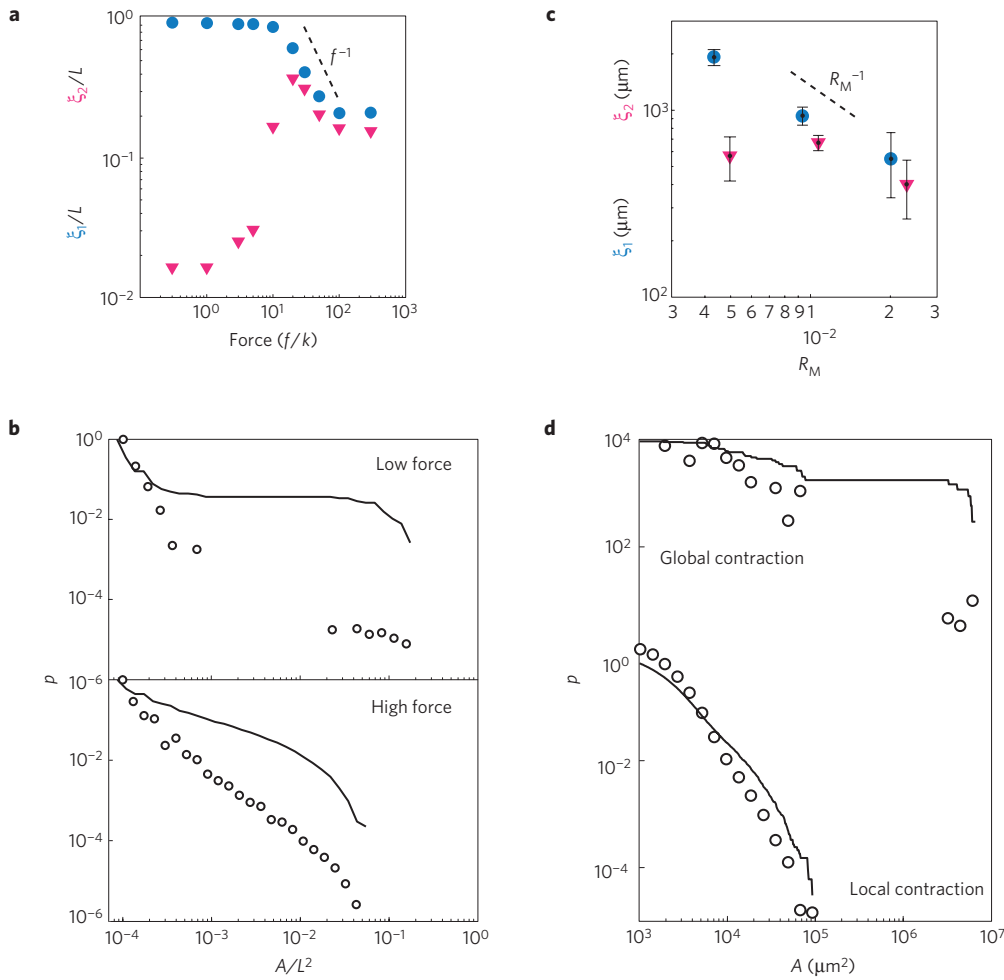


**Figure 4 | Simulation and experiment both show that increased motor force reduces cluster size. a**, Dependence of  $\xi_1$  (blue circles) and  $\xi_2$  (pink triangles) on force  $f$  in simulation. Dashed line depicts  $f^{-1}$ . **b**, Histogram (circles) and complementary cumulative probability distribution (solid lines) of cluster areas,  $a/L^2$ , for low force ( $f/k = 3$ ) and high force ( $f/k = 50$ ). **c**, Dependence of  $\xi_1$  (blue circles) and  $\xi_2$  (pink triangles) on myosin molar ratio, given by  $R_M$ , in experiment. The crosslink molar ratio is fixed at  $R_C = 0.02$ . Error bars denote standard errors of the mean for repeat experiments: 5, 14, and 5 experiments for  $R_M = 0.005, 0.01$ , and  $0.02$ , respectively. Dashed line depicts  $R_M^{-1}$ . **d**, Histogram (circles) and complementary cumulative probability distribution (solid lines) of cluster areas,  $A$ , for networks with varying  $R_M$  in the global and local contraction regimes. For the  $\xi_1$ - $\xi_2$  plot and cluster size distributions of the critically connected regime, see Supplementary Fig. S3.

work<sup>39</sup>, we estimate  $\tau_{\text{relax}} \sim 0.1$ – $1$  s, which acts as an upper bound: forces can cause faster relaxation. Therefore in the absence of crosslink tension,  $\tau_{\text{off}} > \tau_{\text{relax}}$ .

We now consider how these timescales respond to the two limits of local and global contraction. In the global contraction limit,  $f$  and  $T$  are small, and  $\tau_{\text{off}} > \tau_{\text{relax}}$  holds: once a crosslink unbinds, the network fully relaxes before the next crosslink unbinds. This well-known limit corresponds to a quasistatic process<sup>40</sup>. Boundary conditions determine how the network evolves in this limit: networks fixed at rigid boundaries build up stress and rupture via the nucleation of a large crack at a microscopic flaw, reminiscent of Griffith's criterion<sup>41</sup>. Unanchored networks contract affinely, or drive shape changes when coupled to deformable boundaries<sup>42</sup>.

In the opposite limit of local contraction,  $f$  and  $T$  are large, and the network satisfies  $\tau_{\text{off}} < \tau_{\text{relax}}$ : strong internal driving causes crosslinks to unbind quickly. Many cracks that rupture the network into clusters form across the whole network, rather than nucleating at a single flaw. The presence of a finite viscosity in our model is essential for this behaviour (see Supplementary Information).

In between the two limits of global and local contractions, we find critically connected networks with a scale-free distribution of clusters. For zero force, this regime is narrow and centred around

the critical point. As forces increase, this regime broadens and shifts to higher connectivities. This rightward shift reflects an asymmetry where motor activity reduces connectivity, rather than increasing it. The broadening can be understood by the motor-induced reduction of connectivity to a lower connectivity state at which the network can no longer bear stress and crosslink unbinding stops. Strikingly, the myosin-driven bond dilution process is different from random dilution: network restructuring leads to a state of connectivity above that of the connectivity critical point (Supplementary Fig. S5).

Intriguingly, robust critical behaviour has been demonstrated in many biological systems<sup>43–47</sup>. Internal driving could underlie robust criticality<sup>48</sup>, but so could other mechanisms, including natural selection<sup>49,50</sup>. Disentangling these mechanisms cannot be addressed by studying living systems alone. Here we report robust criticality in a minimal model system and show that internal driving is directly responsible. These results may help explain criticality in other biological contexts and may prove useful in designing the physical properties of synthetic active materials, which have recently become available<sup>51</sup>.

Our framework offers a minimal microscopic mechanism of actomyosin contraction, which is ubiquitous in biology. Myosin-driven cytoskeletal ruptures contribute to normal cell division<sup>52</sup>,

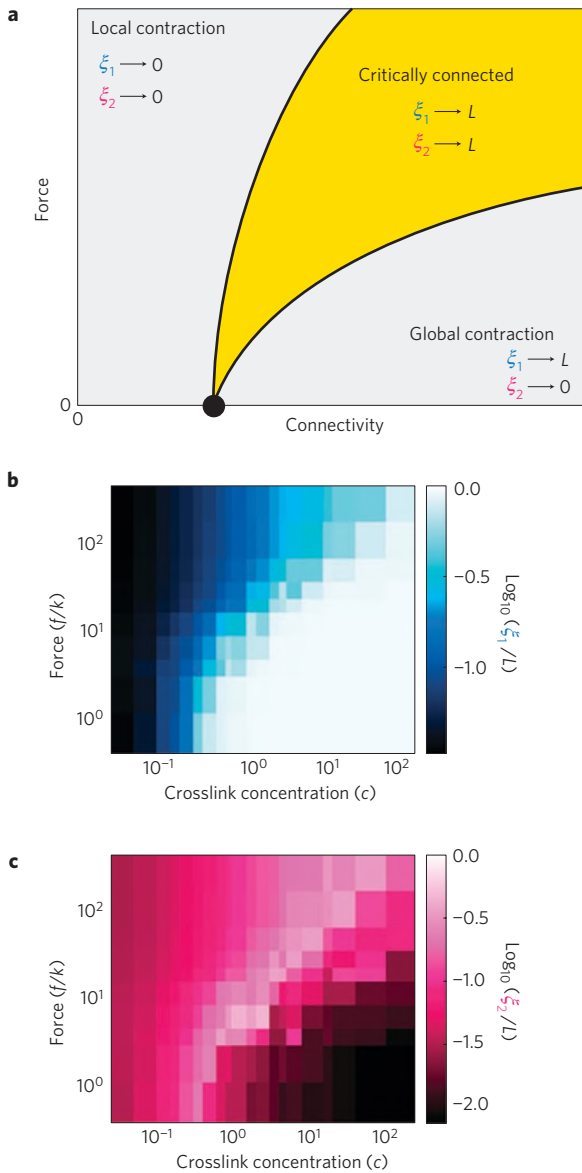


**Figure 5 | The critically connected regime broadens with increasing force.** **a**, Schematic of the proposed phase diagram in force-connectivity space, where the critically connected regime separates the local contraction and global contraction regimes. **b,c**, Dependence of  $\xi_1$  (**b**) and  $\xi_2$  (**c**) simulated over a broad range of force and connectivity.

but also to developmental defects in fly embryos<sup>53</sup>. Consistent with our findings, decreased connectivity caused dramatic rupture of the ventral furrow into clusters of cells in developing fly embryos. We anticipate that our framework applies more generally to epithelial tissues<sup>54,55</sup>, where a supracellular actomyosin network transmits forces over tissue length scales.

## Methods

**Protein preparation.** Actin and myosin were prepared from rabbit psoas skeletal muscle (Supplementary Information). Myosin II was labelled with Alexa Fluor 488 NHS ester (Invitrogen); actin was labelled with Alexa Fluor 594 carboxylic acid, succinimidyl ester<sup>16</sup>. Recombinant mouse fascin was prepared from T7 pGEX *Escherichia coli*<sup>56</sup>.

**Sample preparation.** Samples were mixed to yield a final buffer composition of 20 mM imidazole pH 7.4, 50 mM potassium chloride, 2 mM magnesium chloride, 1 mM dithiothreitol, and 0.1 mM adenosine triphosphate (ATP). Furthermore, 1 mM Trolox, 2 mM protocatechuic acid, and 0.1  $\mu$ M protocatechuate

3,4-dioxygenase were added to minimize photobleaching. The ATP level was held constant by the addition of 10 mM creatine phosphate disodium and 0.1 mg ml<sup>-1</sup> creatine kinase. The actin concentration was held constant at 12  $\mu$ M (0.5 mg ml<sup>-1</sup>). Freshly mixed actomyosin solutions were loaded into polyethylene-glycol-passivated flowcells with a geometry of  $2.5 \times 2.5 \times 0.1$  mm<sup>3</sup> (see Supplementary Information) and sealed with either Baysilone silicone grease (Bayer, Leverkusen) or uncured PDMS (Dow Chemicals, Midland). The time evolution of the network structure was observed with a Nikon PlanFluor 4x objective (NA 0.13), which allows the network to fit entirely within the objective's field of view.

**Contraction assay.** Networks are formed by initiating actin filament polymerization, which results in a semiflexible polymer meshwork with a pore size of  $\sim 0.4$   $\mu$ m. We control the motor activity by adding different amounts of myosin motors, expressed in terms of the myosin-to-actin molar ratio,  $R_M = [\text{myosin}] / [\text{actin}]$ . We control the network connectivity by adding different amounts of the crosslink fascin, which can simultaneously bind to two neighbouring actin filaments. We express the crosslink density in terms of the fascin-to-actin molar ratio,  $R_C = [\text{fascin}] / [\text{actin}]$ . To ensure that we can observe motor-driven contraction on all scales, from microscopic to macroscopic, we prepare networks in customized flow-cells, which fit entirely in the field-of-view of the  $4\times$  objective of a confocal microscope (see Supplementary Information). To track the temporal evolution of the networks, we acquire time-lapse movies starting from 1 min after the initiation of actin polymerization, where the solution is still homogeneous, until 2 h afterwards.

**Image analysis.** Cluster sizes were determined by a customized algorithm, implemented in MATLAB. Time-lapse images of contracting actomyosin networks were analysed, starting from the final acquired frame. Cluster evolution, determined from Voronoi diagrams of myosin foci, was tracked by looping the algorithm backwards in time (Supplementary Information).

Definition of  $\xi_1$  and  $\xi_2$ . For experimental results, we measure the areas  $a_i$  of the initial network that contract together, which we define as clusters. We define  $\xi_1$  as the weighted mean of cluster sizes  $l_i$  (square root of area), in analogy to the definition of the correlation length from percolation theory<sup>26</sup>:

$$\xi_1 := \sum_i l_i a_i^2 / \sum_i a_i^2$$

This length scale is dominated by the largest cluster. We furthermore define  $\xi_2$  in analogy to percolation theory:

$$\xi_2 := \sum_i' l_i a_i^2 / \sum_i a_i^2$$

where  $\sum_i'$  denotes summation over all clusters except for the largest cluster, as well as long edge clusters (Supplementary Information). This length scale is dominated by the second-largest cluster.

For simulation results,  $\xi_1$  is given by the square root of the harmonic average of the largest cluster of each disorder realization, and  $\xi_2$  is given by the square root of the harmonic-averaged areas of all clusters. In the case of a probability density with two length scales (cf. Supplementary Fig. S2, bottom panel), the definitions of  $\xi_1$  and  $\xi_2$  coincide with the large and the small scale, respectively. Simulations were performed over 10–100 disorder realizations for each set of parameters (Supplementary Information).

## References

- Fielding, S. M., Cates, M. E. & Sollich, P. Shear banding, aging and noise dynamics in soft glassy materials. *Soft Matter* **5**, 2378–2382 (2009).
- Vissers, T., van Blaaderen, A. & Imhof, A. Band formation in mixtures of oppositely charged colloids driven by an ac electric field. *Phys. Rev. Lett.* **106**, 228303 (2011).
- Weeks, E., Crocker, J., Levitt, A., Schofield, A. & Weitz, D. Three-dimensional direct imaging of structural relaxation near the colloidal glass transition. *Science* **287**, 627–631 (2000).
- Corté, L., Chaikin, P. M., Gollub, J. P. & Pine, D. J. Random organization in periodically driven systems. *Nature Phys.* **4**, 420–424 (2008).
- Van Hecke, M. Jamming of soft particles: Geometry, mechanics, scaling and isotacticity. *J. Phys. Condens. Matter* **22**, 033101 (2009).
- Jülicher, F., Kruse, K., Prost, J. & Joanny, J.-F. Active behavior of the cytoskeleton. *Phys. Rep.* **449**, 3–28 (2007).
- Zemel, A., De, R. & Safran, S. A. Mechanical consequences of cellular force generation. *Curr. Opin. Solid St. M.* **15**, 169–176 (2011).
- Nédélec, F. J., Surrey, T., Maggs, A. C. & Leibler, S. Self-organization of microtubules and motors. *Nature* **389**, 305–308 (1997).

9. Sanchez, T., Chen, D. T. N., DeCamp, S. J., Heymann, M. & Dogic, Z. Spontaneous motion in hierarchically assembled active matter. *Nature* **491**, 431–434 (2012).
10. Mizuno, D., Tardin, C., Schmidt, C. F. & MacKintosh, F. C. Nonequilibrium mechanics of active cytoskeletal networks. *Science* **315**, 370–373 (2007).
11. Koenderink, G. H. *et al.* An active biopolymer network controlled by molecular motors. *Proc. Natl Acad. Sci. USA* **106**, 15192–15197 (2009).
12. Joanny, J.-F. & Prost, J. Active gels as a description of the actin-myosin cytoskeleton. *HFSP J.* **3**, 94–104 (2009).
13. Wang, S. & Wolynes, P. G. Tensegrity and motor-driven effective interactions in a model cytoskeleton. *J. Chem. Phys.* **136**, 145102 (2012).
14. Backouche, F., Haviv, L., Groswasser, D. & Bernheim-Groswasser, A. Active gels: Dynamics of patterning and self-organization. *Phys. Biol.* **3**, 264–273 (2006).
15. Smith, D. *et al.* Molecular motor-induced instabilities and cross linkers determine biopolymer organization. *Biophys. J.* **93**, 4445–4452 (2007).
16. Soares e Silva, M. *et al.* Active multistage coarsening of actin networks driven by myosin motors. *Proc. Natl Acad. Sci. USA* **108**, 9408–9413 (2011).
17. Köhler, S., Schaller, V. & Bausch, A. R. Structure formation in active networks. *Nature Mater.* **10**, 462–468 (2011).
18. Bendix, P. M. *et al.* A quantitative analysis of contractility in active cytoskeletal protein networks. *Biophys. J.* **94**, 3126–3136 (2008).
19. Köhler, S. & Bausch, A. R. Contraction mechanisms in composite active actin networks. *PLOS One* **7**, e39869 (2012).
20. Wang, S. & Wolynes, P. G. Active contractility in actomyosin networks. *Proc. Natl Acad. Sci. USA* **109**, 6446–6451 (2012).
21. Wyart, M., Liang, H., Kabla, A. & Mahadevan, L. Elasticity of floppy and stiff random networks. *Phys. Rev. Lett.* **101**, 215501 (2008).
22. Broedersz, C. P., Mao, X., Lubensky, T. C. & MacKintosh, F. C. Criticality and isostaticity in fibre networks. *Nature Phys.* **7**, 983–988 (2011).
23. Sheinman, M., Broedersz, C. P. & MacKintosh, F. C. Nonlinear effective-medium theory of disordered spring networks. *Phys. Rev. E* **85**, 021801 (2012).
24. Sheinman, M., Broedersz, C. & MacKintosh, F. Actively stressed marginal networks. *Phys. Rev. Lett.* **109**, 238101 (2012).
25. Weber, C., Schaller, V., Bausch, A. & Frey, E. Nucleation-induced transition to collective motion in active systems. *Phys. Rev. E* **86**, 030901 (2012).
26. Stauffer, D. & Aharony, A. *Introduction to Percolation Theory* (Taylor Francis, 1994).
27. Clauset, A., Shalizi, C. R. & Newman, M. E. J. Power-law distributions in empirical data. *SIAM Rev.* **51**, 661–703 (2009).
28. Haviv, L., Gillo, D., Backouche, F. & Bernheim-Groswasser, A. A cytoskeletal demolition worker: Myosin II acts as an actin depolymerization agent. *J. Mol. Biol.* **375**, 325–330 (2008).
29. Murrell, M. P. & Gardel, M. L. F-actin buckling coordinates contractility and severing in a biomimetic actomyosin cortex. *Proc. Natl Acad. Sci. USA* **109**, 20820–20825 (2012).
30. Vogel, S. K., Petrasek, Z., Heinemann, F. & Schwill, P. Myosin motors fragment and compact membrane-bound actin filaments. *eLife* **2**, e00116 (2013).
31. Courson, D. S. & Rock, R. S. Actin cross-link assembly and disassembly mechanics for alpha-actinin and fascin. *J. Biol. Chem.* **285**, 26350–26357 (2010).
32. Evans, E. & Ritchie, K. Dynamic strength of molecular adhesion bonds. *Biophys. J.* **72**, 1541–1555 (1997).
33. Ishikawa, R., Sakamoto, T., Ando, T., Higashi-Fujime, S. & Kohama, K. Polarized actin bundles formed by human fascin-1: Their sliding and disassembly on myosin II and myosin V *in vitro*. *J. Neurochem.* **87**, 676–685 (2003).
34. Storm, C., Pastore, J. J., MacKintosh, F. C., Lubensky, T. C. & Janmey, P. A. Nonlinear elasticity in biological gels. *Nature* **435**, 191–194 (2005).
35. Chaudhuri, O., Parekh, S. H. & Fletcher, D. A. Reversible stress softening of actin networks. *Nature* **445**, 295–298 (2007).
36. MacKintosh, F. C. & Levine, A. J. Nonequilibrium mechanics and dynamics of motor-activated gels. *Phys. Rev. Lett.* **100**, 018104 (2008).
37. Liverpool, T. B., Marchetti, M. C., Joanny, J.-F. & Prost, J. Mechanical response of active gels. *Europhys. Lett.* **85**, 18007 (2009).
38. Lenz, M., Thoresen, T., Gardel, M. & Dinner, A. Contractile units in disordered actomyosin bundles arise from f-actin buckling. *Phys. Rev. Lett.* **108**, 238107 (2012).
39. Koenderink, G. H., Atakhorrami, M., MacKintosh, F. C. & Schmidt, C. F. High-frequency stress relaxation in semiflexible polymer solutions and networks. *Phys. Rev. Lett.* **96**, 13807 (2006).
40. Heussinger, C. Stress relaxation through crosslink unbinding in cytoskeletal networks. *New J. Phys.* **14**, 095029 (2012).
41. Griffith, A. A. The phenomena of rupture and flow in solids. *Phil. Trans. R. Soc. Lond. A* **221**, 163–198 (1921).
42. Martin, A. C., Kaschube, M. & Wieschaus, E. F. Pulsed contractions of an actin-myosin network drive apical constriction. *Nature* **457**, 495–499 (2009).
43. Camalet, S., Duke, T., Jülicher, F. & Prost, J. Auditory sensitivity provided by self-tuned critical oscillations of hair cells. *Proc. Natl Acad. Sci. USA* **97**, 3183–3188 (2000).
44. Veatch, S. L. *et al.* Critical fluctuations in plasma membrane vesicles. *ACS Chem. Biol.* **3**, 287–293 (2008).
45. Zhang, H. P., Be'er, A., Florin, E. L. & Swinney, H. L. Collective motion and density fluctuations in bacterial colonies. *Proc. Natl Acad. Sci. USA* **107**, 13626–13630 (2010).
46. Mora, T. & Bialek, W. Are biological systems poised at criticality? *J. Stat. Phys.* **144**, 1–35 (2011).
47. Bialek, W. *et al.* Statistical mechanics for natural flocks of birds. *Proc. Natl Acad. Sci. USA* **109**, 4786–4791 (2012).
48. Furusawa, C. & Kaneko, K. Adaptation to optimal cell growth through self-organized criticality. *Phys. Rev. Lett.* **108**, 208103 (2012).
49. Halley, J. D. & Winkler, D. A. Critical-like self-organization and natural selection: Two facets of a single evolutionary process? *BioSystems* **92**, 148–158 (2008).
50. Torres-Sosa, C., Huang, S. & Aldana, M. Criticality is an emergent property of genetic networks that exhibit evolvability. *PLOS Comput. Biol.* **8**, e1002669 (2012).
51. Bertrand, O. J. N., Fygenson, D. K. & Saleh, O. A. Active, motor-driven mechanics in a DNA gel. *Proc. Natl Acad. Sci. USA* **109**, 17342–17347 (2012).
52. Sedzinski, J. *et al.* Polar actomyosin contractility destabilizes the position of the cytokinetic furrow. *Nature* **476**, 462–466 (2011).
53. Martin, A. C. *et al.* Integration of contractile forces during tissue invagination. *J. Cell Biol.* **188**, 735–749 (2010).
54. Schwarz, U. & Safran, S. Elastic interactions of cells. *Phys. Rev. Lett.* **88**, 048102 (2002).
55. Schwarz, U. S. & Gardel, M. L. United we stand—integrating the actin cytoskeleton and cell-matrix adhesions in cellular mechanotransduction. *J. Cell Sci.* **125**, 3051–3060 (2012).
56. Gentry, B. S. *et al.* Multiple actin binding domains of Ena/VASP proteins determine actin network stiffening. *Eur Biophys. J.* **41**, 979–990 (2012).

## Acknowledgements

This work is part of the research programme of the Foundation for Fundamental Research on Matter (FOM), which is part of the Netherlands Organisation for Scientific Research (NWO). G.H.K. and J.A. were funded by a Vidi grant from the Netherlands Organisation for Scientific Research (NWO). We thank M. Kuit-Vinkenoog, M. Preciado-López and F. C. Tsai (AMOLF, Amsterdam, Netherlands) for help with purifications, S. Hansen and R. D. Mullins (UCSF, San Francisco, USA) for the fascin plasmid, K. Miura (EMBL, Heidelberg, Germany) for the Temporal Colour Code ImageJ plugin, as well as C. Broedersz (Princeton University, NJ, USA) and M.A.J. Michels (TU Eindhoven) for insightful discussions.

## Author contributions

J.A. and G.H.K. designed the experiments. J.A. performed the experiments. M.S., A.S., and F.C.M. designed the simulations. M.S. and A.S. performed the simulations. All authors contributed to the writing of the paper.

## Additional information

Supplementary information is available in the [online version of the paper](#). Reprints and permissions information is available online at [www.nature.com/reprints](http://www.nature.com/reprints). Correspondence and requests for materials should be addressed to F.C.M. or G.H.K.

## Competing financial interests

The authors declare no competing financial interests.